ARTICLES
https://doi.org/10.1038/s41550-021-01531-9

nature astronomy

Check for updates

Polarimetric detection of non-radial oscillation modes in the β Cephei star β Crucis

Daniel V. Cotton[1,2,3,4]✉, Derek L. Buzasi[5]✉, Conny Aerts[6,7,8], Jeremy Bailey[3,9], Siemen Burssens[6], May G. Pedersen[6,10], Dennis Stello[9], Lucyna Kedziora-Chudczer[4], Ain De Horta[3], Peter De Cat[11], Fiona Lewis[9], Sai Prathyusha Malla[9], Duncan J. Wright[4] and Kimberly Bott[12]

Here we report the detection of polarization variations due to non-radial modes in the β Cephei star β Crucis. In so doing we confirm 40-year-old predictions of pulsation-induced polarization variability and its utility in asteroseismology for mode identification. In an approach suited to other β Cephei stars, we combine polarimetry with space-based photometry and archival spectroscopy to identify the dominant non-radial mode in polarimetry, f_2, as mode degree $\ell = 3$, azimuthal order $m = -3$ (in the *m*-convention of Dziembowski) and determine the stellar axis position angle as 25 (or 205) ± 8°. The rotation axis inclination to the line of sight was derived as ~46° from combined polarimetry and spectroscopy, facilitating identification of additional modes and allowing for asteroseismic modelling. This reveals a star of 14.5 ± 0.5 $M_\odot$ and a convective core containing ~28% of its mass—making β Crucis the most massive star with an asteroseismic age.

Asteroseismology has revolutionized our knowledge of low- and intermediate-mass stars across their entire evolution, determining fundamental parameters like mass, radius and age, and inferring interior rotation[1–3]. Some of the high-mass stars in the range 8–25 $M_\odot$ are seismically active and known as β Cephei (β Cep) stars[4]. Their pulsation modes are of low radial order and lack recognizable frequency patterns, making mode assignment difficult[5,6]. Identification of the mode degree, ℓ, and azimuthal order, m, are prerequisites for asteroseismic inferences of the stellar interior[7].

Because they are the progenitors of core-collapse supernovae and black holes, there is considerable interest in divining the interior structure of high-mass stars. However, identification of mode wavenumbers (ℓ, m) remains a large challenge for successful asteroseismology. Mode identifications in β Cep stars using multi-band photometry and light curve analysis[8] have proven difficult to achieve from ground-based data, with sometimes decades of effort expended on obtaining unambiguous mode identification in individual stars[9]. Some progress on the asteroseismology of β Cep stars has resulted from extensive multisite campaigns[10,11] and from combined Microvariability and Oscillations of Stars (MOST) space photometry and ground-based spectroscopy[12]. While such combinations of data were insightful for a few β Cep stars, they remain too rare to advance the theory and understanding of their stellar interiors. As polarization is a pseudo-vector quantity, polarimetry potentially offers an advantage over other techniques in that spatial information pertaining to the stellar surface is directly encoded in the signal through the polarization position angle (derived from normalized Stokes vectors Q/I and U/I (refs. [13,14])).

Light scattering from electrons in the atmospheres of hot stars leads to linear polarization, being zero at the centre of the stellar disk but increasing radially to a maximum at the limb of the star, as first predicted by Chandrasekhar[15]. The polarization will average to zero over a spherical star but can be observed if the star deviates from spherical symmetry. Distortion of a star due to non-radial pulsation[8] should therefore lead to temporal polarization variations. Models of these effects were first developed in the 1970s[16,17] and showed how polarization could provide constraints on the pulsation modes[18]. Most attempts to detect polarization signatures in β Cep stars have been unsuccessful[19–21], but Odell[22] has reported a detection of polarization in the large amplitude β Cep star BW Vulpeculae (BW Vul). However, the result is questionable[23] due to the small dataset and the relative imprecision of the instrumentation of the time; it is also inconsistent with the identification of the pulsation as a radial mode[23], which would not produce any polarization.

Modern high-precision polarimeters[24,25] can achieve much better precision than has been possible in past work. These instruments have enabled the detection of long-predicted polarization effects caused by rapid rotation in hot stars[26,27] and shown B stars to have a tendency for higher polarizations in general[28]. In this project, we used the High Precision Polarimetric Instrument 2 (HIPPI-2)[25] co-ordinated with photometric observations by the Transiting Exoplanet Survey Satellite (TESS), which is able to provide high-quality space photometry for pulsating B stars[29].

Results

Between 29 March 2018 and 10 July 2019 a total of 307 linear polarimetric observations were made of β Crucis (β Cru, Mimosa, HD 111123), mostly at the 3.9-m Anglo Australian Telescope (AAT) at Siding Spring Observatory in the SDSS g′ band (Supplementary Fig. 1). So configured, HIPPI-2 can obtain better than 3

[1]Monterey Institute for Research in Astronomy, Marina, CA, USA. [2]Anglo Australian Telescope, Australian National University, Coonabarabran, New South Wales, Australia. [3]Western Sydney University, Penrith-South, New South Wales, Australia. [4]Centre for Astrophysics, University of Southern Queensland, Toowoomba, Queensland, Australia. [5]Department of Chemistry & Physics, Florida Gulf Coast University, Fort Myers, FL, USA. [6]Institute of Astronomy, KU Leuven, Leuven, Belgium. [7]Department of Astrophysics, IMAPP, Radboud University Nijmegen, Nijmegen, the Netherlands. [8]Max Planck Institute for Astronomy, Heidelberg, Germany. [9]School of Physics, UNSW Sydney, Sydney, New South Wales, Australia. [10]Kavli Institute for Theoretical Physics, University of California, Santa Barbara, CA, USA. [11]Royal Observatory of Belgium, Brussels, Belgium. [12]Department of Earth and Planetary Science, University of California, Riverside, CA, USA. ✉e-mail: dc@mira.org; dbuzasi@fgcu.edu

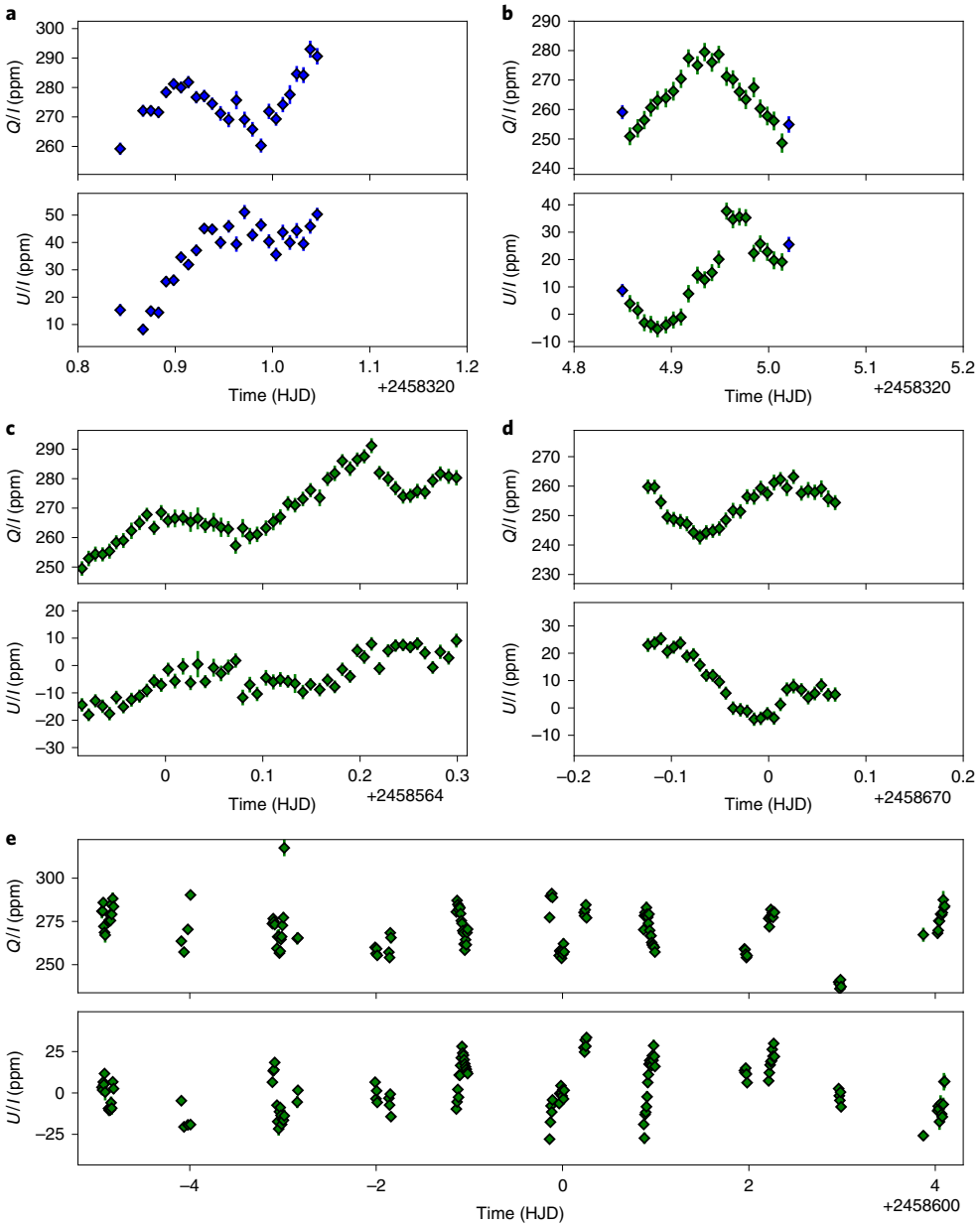

Fig. 1 | β Cru time-series examples. a–e, Polarimetric observations of β Cru are shown as pairs of time series for *Q*/*I* (upper panels) and *U*/*I* (lower panels) for four single nights (**a**–**d**), and a 10-night run (**e**) to demonstrate the polarimetric variability on short timescales. Unfiltered (clear) observations are shown in blue and SDSS g′ observations in green. The plotted uncertainties are the nominal 1σ errors, which are a combination of photon shot noise and an instrumental 'positioning error'[25].

parts-per-million (ppm) precision in a short exposure (see Methods for details). The data include a number of sets of observations spanning half a night or more, which all show the polarization to vary smoothly in a periodic way with an amplitude of tens of ppm (Fig. 1).

TESS observed β Cru in 2-minute cadence for 27 days between 22 April 2019 and 21 May 2019 and thus overlaps the ground-based polarimetric observations in time (Methods). Together these datasets, along with archival data from the Wide Field Infrared Explorer (WIRE), Hipparcos and ground-based spectroscopy were used to carry out a joint frequency analysis (Methods, Fig. 2 and Supplementary Fig. 2). Such an analysis identifies signals due to pulsations, but also other repeating signals that could be associated with, for instance, rotation.

The frequency analysis reveals (at >4σ significance, that is, a signal-to-noise ratio, SNR, larger than 4) 11 distinct pulsation frequencies present in more than 1 dataset, 6 more than previously identified for β Cru (a full list is given in Table 1). There are significant differences between the WIRE and TESS amplitudes, which may be indicative of time-varying mode amplitudes (Supplementary Information), common for multiperiodic stars with heat-driven pulsations[30]. These are the type of modes excited in the β Cep stars via the κ mechanism[4]. Table 1 also contains a column listing frequencies for fits to the combined WIRE + TESS dataset. Any frequency appearing elsewhere in this is included in this column. Our motivation for including this column is that if frequencies and amplitudes are stable and not aliases, then the long, combined time series has the potential to produce higher precision frequencies.

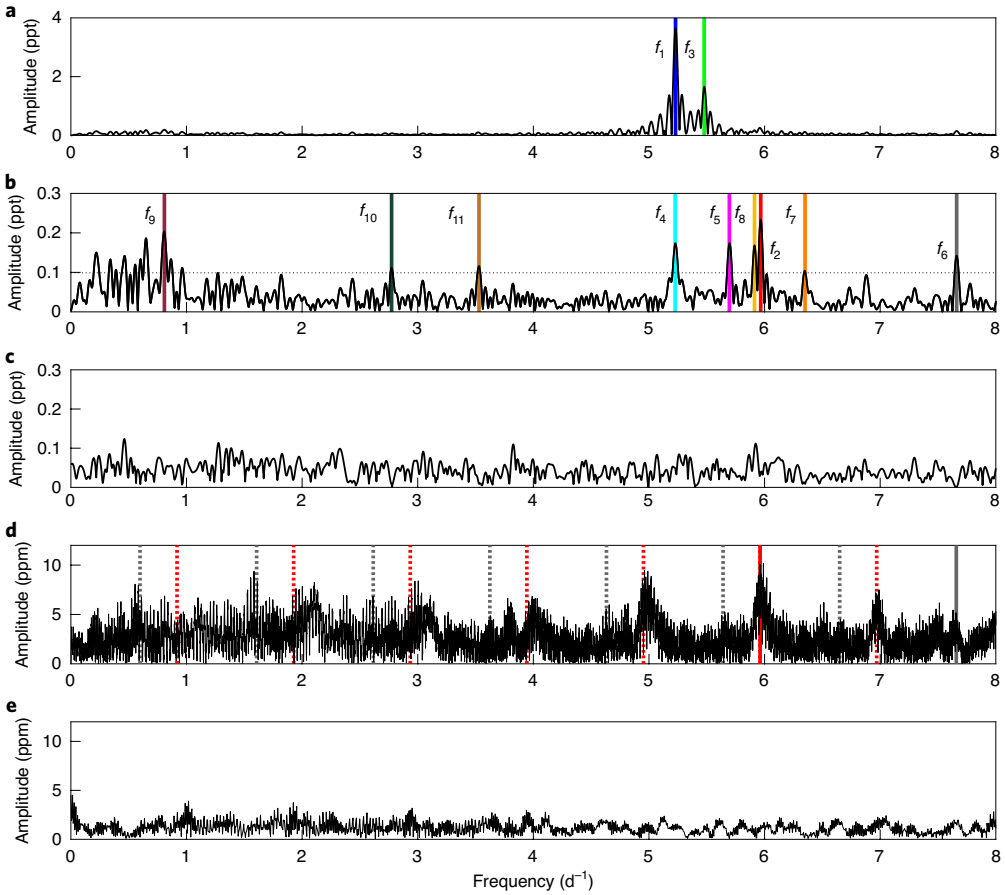

Fig. 2 | Selected amplitude spectra for β Cru. a, The amplitude spectrum derived from the TESS time series for $f \in [0, 8]\,\mathrm{d}^{-1}$. Coloured vertical lines illustrate the two oscillation modes with the largest amplitudes; other frequencies are not obvious in the amplitude spectrum until prewhitening has been performed. **b**, The amplitude spectra derived from the TESS time series (in black), after prewhitening for f_1 and f_3. Peak locations are identified by coloured vertical lines. The horizontal dotted line indicates SNR = 4. **c**, The TESS amplitude spectrum after 23 identified modes have been prewhitened, as discussed in the text. While some peaks remain at the <0.1 ppt level, none of these reaches our required significance level. **d**, The amplitude spectrum from HIPPI-2 *Q*/*I* polarimetry. The complex quasiperiodic structure visible is due to diurnal (and other) aliasing and illustrates the value of using multiple datasets to determine which peaks are 'real'. Here the red and grey vertical lines mark the two detected oscillation modes in this dataset, while the matching dotted lines show the locations of predicted $\pm 1, 2, 3, \ldots\,\mathrm{d}^{-1}$ alias peaks. **e**, The same HIPPI-2 *Q*/*I* amplitude spectrum after prewhitening 23 frequencies. The *U*/*I* spectra are similar and are shown in Supplementary Fig. 2. Note: 1 ppt = 1000 ppm.

Amongst the detected frequencies are two in the polarimetric data corresponding to both photometric and spectroscopic frequencies. The first of these, which we detect in both linear Stokes parameters, is at $5.964\,\mathrm{d}^{-1}$ and has been previously detected and assigned as f_2 (refs. [5,31,32]). In *Q*/*I* and *U*/*I*, the amplitude of this mode is 7.08 ± 0.91 ppm and 5.78 ± 0.97 ppm, respectively, roughly a hundredth of its WIRE amplitude and a 35th of its TESS amplitude. All the detected modes of β Cru have lifetimes much longer than the individual datasets, as revealed from Lorentzian fits to the power spectra, and are thus confirmed to be undamped. The second frequency found in the polarimetric data is at $7.659\,\mathrm{d}^{-1}$ (f_6) and is a newly found mode; we only detect it in *Q*/*I* with an amplitude of 2.89 ± 0.62 ppm, about a 50th of its TESS amplitude.

The uncertainty in the frequencies based on the polarimetry alone is an order of magnitude larger than the frequency determinations from TESS, so we refit the polarimetric data, $S = Q/I$ or U/I, as a sinusoid of the form $S(t) = A\sin(2\pi ft + \phi)$, fixing the frequency to the TESS value for $f_2 = 5.964(5)\,\mathrm{d}^{-1}$. This produced amplitudes $A_\mathrm{Q} = 8.76 \pm 0.86$ ppm and $A_\mathrm{U} = 7.97 \pm 0.94$ ppm, and phase differences from the TESS photometry of $\phi_\mathrm{Q} - \phi = -0.817 \pm 0.113$ rad and $\phi_\mathrm{U} - \phi = -2.259 \pm 0.167$ rad respectively, as shown in Fig. 3a-c. Taking $2A$ as the polarimetric variation expected from f_2, this accounts for a third of the typical variability on a night (Fig. 1), which suggests that further modes may exist below our noise threshold. Alternatively, minor discrepancies in the calibrations between runs and/or inaccuracies in the zero-point offsets, as seen elsewhere[33], could decrease the amplitudes.

Pulsation-induced total light intensity, spectral line velocity and polarization variations are driven by the cumulative effects of local changes in temperature, gravity and geometry due to the non-radial displacements caused by the modes. Watson[18], whose notation we adopt in this paper, developed the most sophisticated analytical model of polarization in pulsating stars, following the same theoretical approach employed by Dziembowski[34] for photometry.

We followed the procedures outlined by Watson[18] in applying the analytical model to f_2; the details are given in the Methods. In summary, we first noted that $\phi_\mathrm{U} - \phi \simeq -\pi/2$; this is one of only two allowed values, indicating that the polarization rotates anti-clockwise on the sky (north through east), and informing the sign of m. We next rotate the polarization between Stokes parameters so that in the model frame (denoted $^\mathrm{M}$) the phase difference $\phi^\mathrm{M}_{\mathrm{Q}\lambda} - \phi_\lambda$ is either 0 or π. The angle of the rotation, $2\Phi_\chi$, is twice

Table 1 | Significant frequencies found for β Cru

ID	2002 WIRE	WIRE	TESS	$\langle v \rangle$	$\langle v^2 \rangle$	Q/I	U/I	Hipparcos	WIRE+TESS
	f (d^{-1})	f (d^{-1})	f (d^{-1})	f (d^{-1})	f (d^{-1})	f (d^{-1})	f (d^{-1})	f (d^{-1})	f (d^{-1})
		A (ppm)	A (ppm)	A (km s^{-1})	A (km^2 s^{-2})	A (ppm)	A (ppm)	A (ppm)	A (ppm)
f_1	5.228(1)	5.229(3)	5.2298(6)	5.2298(2)	5.2298(2)			5.22977(5)	5.229776(1)
		3523(50)	3639(16)	0.69(4)	441(37)			7291(73)	3705(17)
f_2	5.956(7)	5.96(1)	5.964(5)	5.9636(2)		5.964(1)	5.964(2)		5.96364(2)
		634(47)	231(10)	0.67(4)		7.08(91)	5.78(97)		251(12)
f_3	5.477(2)	5.478(6)	5.4777(8)	5.477(2)	5.4777(2)				5.477750(3)
		2730(28)	1641(10)	0.47(5)	412(37)				1872(10)
f_4		5.22(2)	5.216(9)	5.21628(9)	5.2162(2)				5.2162(6)
		311(34)	144(10)	0.61(5)	448(34)				78(11)
f_5			5.699(9)		5.699(13)				5.6977(3)
			119(10)		302(36)				141(10)
f_6			7.661(8)		7.6605(6)	7.659(4)			7.6605(3)
			143(9)		255(38)	2.89(62)			99(9)
f_7			6.36(1)		6.359(4)				6.3596(6)
			89(9)		336(39)				57(9)
f_8			5.92(1)		5.9229(1)				5.9229(6)
			90(9)		534(36)				55(9)
f_9		0.82(3)	0.819(7)						0.81902(2)
		316(44)	177(10)						209(12)
f_{10}	2.785(13)	2.78(2)	2.78(1)						2.77786(3)
		236(31)	112(9)						131(10)
f_{11}	3.527(13)	3.529(17)	3.53(1)						3.52863(3)
		368(34)	118(10)						122(10)
Δf	0.057	0.057	0.039	0.00024	0.00024	0.0021	0.0021	0.00091	0.00014

Frequencies shown are those for which an SNR > 4 detection was made in 2 or more independent datasets. The polarimetric data, Q/I and U/I are derived from HIPPI-2 observations. The spectroscopic data giving $\langle v \rangle$ and $\langle v^2 \rangle$ were acquired with European Southern Observatory's Coudé Auxiliary Telescope / Coudé Echelle Spectrometer (CAT/CES) instrumentation[5]. The rightmost column shows frequency and amplitude determinations based on the combination of the WIRE and TESS time series, which provides the longest temporal baseline and hence the most precise frequency determination; as those two missions were well-separated in time and had different bandpasses, the amplitudes derived from the combined time series should be considered as illustrative only. Mode detections and frequencies from the original 2002 analysis[32] of the WIRE data are also shown for reference. Mode identifications (IDs) for f_1–f_8 reflect assignments previously occurring in the literature and/or used in our spectroscopic mode identification (Methods), while new IDs f_9–f_{11} are assigned in order of increasing frequency. The last row of the table gives the nominal frequency resolution for each dataset, estimated from each time-series length T as $\Delta f = 1/T$; this is most meaningful for the photometric time series, which have high duty cycles.

the position angle of the stellar axis on the sky (or twice the position angle plus π, since direction is ambiguous in polarimetry); the procedure is depicted in Fig. 3. Finally, the amplitudes of the fits to the pulsations in the rotated Stokes parameters, $A^{\rm M}_{{\rm Q}\lambda}$ and $A^{\rm M}_{{\rm U}\lambda}$, along with photometric amplitude, $A^{\rm M}_{\lambda}$, eliminate some (ℓ, m) combinations and restrict the inclinations of others through the amplitude ratios $A^{\rm M}_{{\rm U}\lambda}/A^{\rm M}_{{\rm Q}\lambda}$ and $A^{\rm M}_{{\rm Q}\lambda}/A^{\rm M}_{\lambda}$ as shown in Fig. 4.

As a consequence of symmetry, only $\ell \geq 2$ modes can produce any significant polarization (Methods), and modes with $\ell \geq 5$ are not known to be prominent in photometry of slowly rotating β Cep stars[35,36], and thus are unlikely to be identified in the joint frequency analysis; therefore, we restricted our analysis to $2 \leq \ell \leq 4$ (see also the Supplementary Information for further arguments). Then, as can be seen in Fig. 4, using the TESS photometry, f_2 is limited to six possible modes, each associated with a distinct inclination range; these are: $(2,-2)$, $i = 7^{+4}_{-2}{}^{\circ}$; $(3,+1)$, $i = 66^{+9}_{-1}{}^{\circ}$; $(3,-2)$, $i = 20^{+8}_{-4}{}^{\circ}$; $(3,-3)$, $i = 37^{+18}_{-8}{}^{\circ}$; $(4,-2)$, $i = 11^{+5}_{-3}{}^{\circ}$; and $(4,-4)$, $i = 27^{+13}_{-6}{}^{\circ}$. As described in the Methods, we have cautiously used 3σ errors to determine these ranges and the position angles, which for the $(3,+1)$ solution corresponds to $\Phi_\chi = 115 \pm 8°$ and for the other modes to $\Phi_\chi = 25 \pm 8°$. This may still seem like a large number of possibilities, but the result allows us to very usefully refine our subsequent line-profile analysis.

Stellar oscillations affect spectral line profiles dominantly through changes in the velocity field, although temperature changes may also be involved. The profile due to one mode, $p_{\rm spec}(\lambda, t)$, is described by four mode-dependent parameters, ℓ, m, A_λ and ϕ_λ, and two mode-independent parameters, i and $v\sin i$ — the projected rotational velocity — (ref. [8]). Per additional mode and per wavelength bin λ, four extra free parameters occur in the expression for $p_{\rm spec}(\lambda, t)$ in the approximation of linear oscillation theory. The inclination constraint from polarimetry offers a major reduction in the parameter space to consider for the spectroscopic mode identification. We carried out a line-profile analysis based on the pixel-by-pixel method[37], using the Frequency Analysis and Mode Identification for Asteroseismology (FAMIAS) program[38] to detect and identify the modes present in archival data of β Cru (Methods) of the 4,552.6 Å Si III line. Eight frequencies from Table 1 have significant amplitudes and phases across the line profiles and are shown in Fig. 5.

Three modes have amplitudes dominant over the other five in the spectroscopic data: they are frequencies f_2, f_8 and f_1, which are detected at $>10\sigma$. Nevertheless, we performed mode identification for all eight modes, initially adopting the restriction that $i < 75°$. We then eliminated those solutions that were inconsistent with the polarimetric results; first by restricting the inclination to the

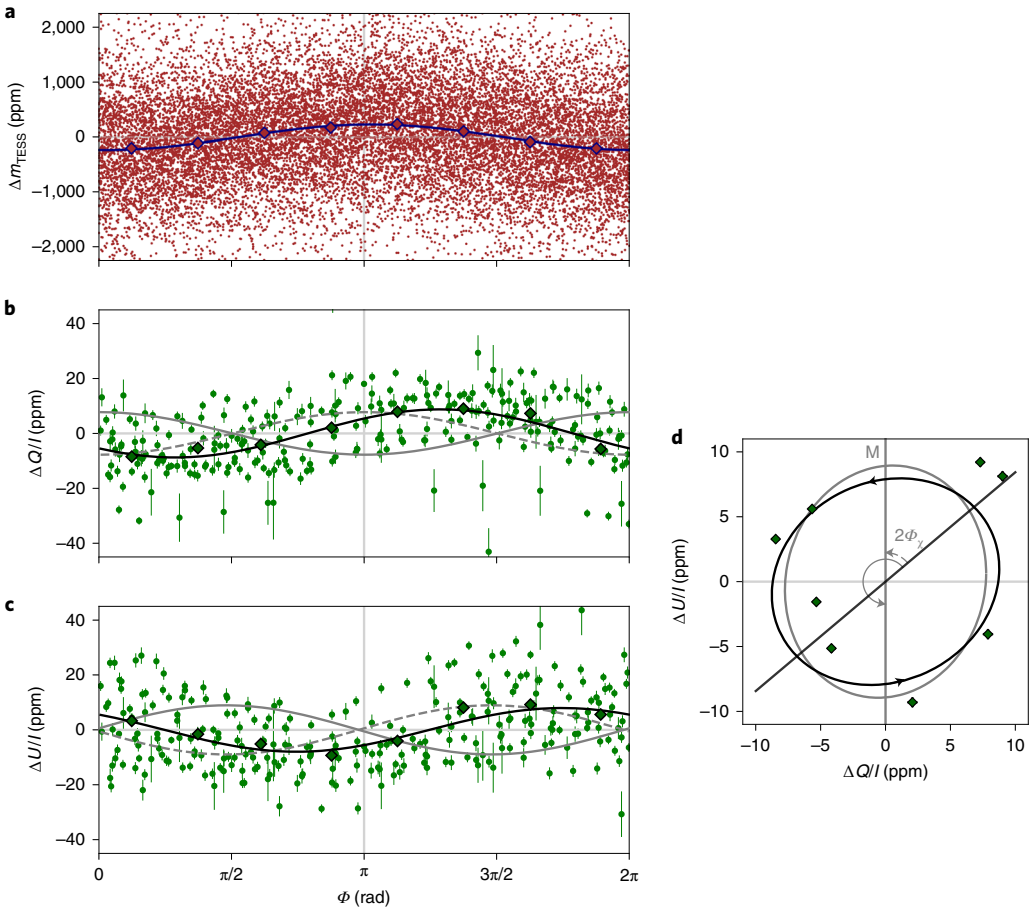

Fig. 3 | Photometric and polarimetric data phase-folded to f_2 for β Cru. a–c, The change in Q/I (**b**) and U/I (**c**) data from the error weighted means (266.5 ± 0.2 ppm and 3.1 ± 0.2 ppm) are shown as green dots (the plotted uncertainties are the nominal 1σ errors, which are a combination of photon shot noise and an instrumental 'positioning error'[25]). Similarly, the photometric data from TESS are shown as brown dots (**a**). The sinusoidal fits to the photometric and polarimetric data, locked at the TESS-derived frequency $f_2 = 5.964$ d^{-1}, are shown as the solid blue and black lines, respectively. The diamonds in each plot represent the data binned in increments of $\pi/4$ rad. **d**, The phase-binned polarimetric data as a Q-U diagram (the formal errors are the size of the data points). Projected onto this plane, the sinusoidal fit becomes a polarization ellipse; the black arrows indicate the direction of data progress with phase, which is the same as it is on the sky. Rotating the ellipse so that major and minor axes correspond to the $\Delta U/I$ and $\Delta Q/I$ axes (or, in general, vice versa) aligns the data to the frame of the analytical model of Watson[18], labelled M, and shown in grey. The rotation angle required is twice the position angle of the stellar axis (Φ_χ). The two allowed solutions correspond to $\phi^{M}_{Q\lambda} - \phi_\lambda = 0$ (dashed grey line) and $\phi^{M}_{Q\lambda} - \phi_\lambda = \pi$ (solid grey line) in panels **b** and **c**. The values of $A^{M}_{Q\lambda}$ and $A^{M}_{U\lambda}$ then correspond to the intersection of the rotated polarization ellipse with the axes of the Q-U diagram.

ranges allowed for f_2 as described above (Fig. 6 shows how applying this constraint alone cuts down the allowed solutions significantly), then subsequently to accommodate the detection of A^{M}_{U} in f_6 and the non-detections of other frequencies in polarimetry. The outcome of the combined mode identification is demonstrated in Supplementary Tables 6 and 7 and reveals a fully consistent solution for $(\ell_2, m_2) = (3, -3)$ and $v \sin i = 14 \pm 2$ km s^{-1}. The strongest mode in photometry, f_1, is found to be a dipole mode in agreement with previous results[6]. We were also able to place restrictions on the mode identification of f_8 and the five lower-amplitude modes detected in the spectroscopy, although the uniqueness for those is not guaranteed as several solutions are almost equivalent (Methods). For the mode with frequency f_6, a combination of spectroscopy and polarimetry delivered additional information (see the Supplementary Information, including Supplementary Fig. 3, for details of its assignment and also constraints placed on the remaining frequencies by their non-detection in polarimetry).

Few β Cep stars have been modelled asteroseismically with inferred values of the mass, radius, age and convective-core mass, due to lack of mode identification. We performed such initial modelling for β Cru, based on a neural network trained for radial, dipole and quadrupole modes[39]. We applied this network to the star's two lowest degree $\ell \leq 2$ modes (f_1 and f_5). The results are presented in Supplementary Figs. 4 and 5 and reveal an 11.3 ± 1.6 million-year-old star of 14.5 ± 0.5 $M_\odot$ with a central hydrogen mass fraction in the range [0.30, 0.33], having a convective core of ~28 ± 3% of its total mass and slow surface rotation with a period between 13 and 17 days. The rotation period is not detected in the space photometry, possibly because it falls in the low-frequency regime of the spectrum (Fig. 2).

Discussion

Previously, it has proven difficult to measure stellar pulsations polarimetrically. Here, using the most precise optical astronomical polarimeter available, we have been able to detect the signatures of two modes in β Cru with small polarimetric amplitudes. A number of further modes are predicted to have polarimetric amplitudes just below the detection threshold, which is the motivation for extending our observations and also for developing more sensitive instruments. Additionally, the calculations presented in Fig. 4

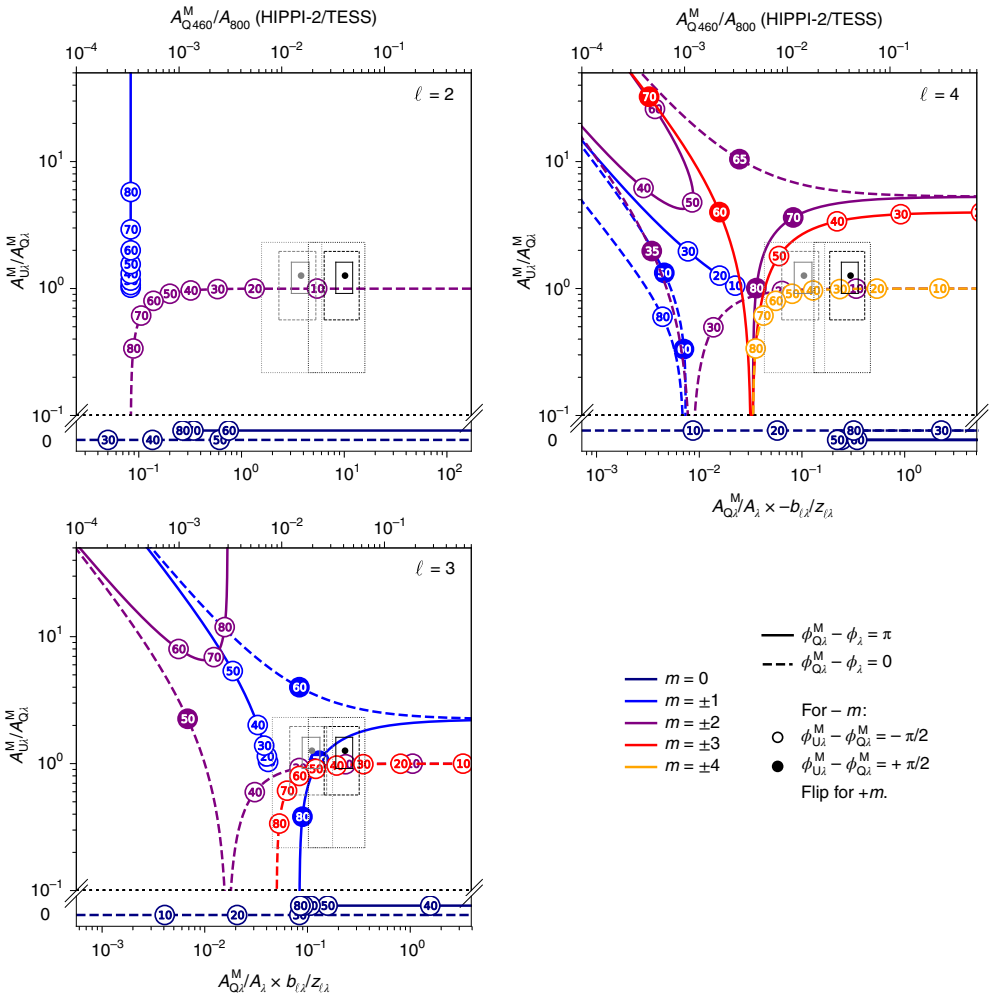

Fig. 4 | Polarimetric mode determination diagrams for the f_2 mode of β Cru. Allowed modes and observational data are shown in terms of the ratios of polarimetric amplitudes ($A^{M}_{U\lambda}/A^{M}_{Q\lambda}$) and polarimetric to photometric amplitudes ($A^{M}_{Q\lambda}/A_{\lambda}$, dimensionless units). Mapped onto the upper-left ($\ell = 2$), lower-left ($\ell = 3$) and upper-right ($\ell = 4$) panels are the allowed m values, where the numbers within the circles indicate stellar inclination. For $m = 0$, note that $A^{M}_{U\lambda}/A^{M}_{Q\lambda} = 0$ and the offsets in their display are for clarity only. The observational ratios for f_2 shown are those of HIPPI-2 g′ (460 nm) polarimetric data and TESS (800 nm, black dot) or WIRE (600 nm, grey dot) photometric data; 1-, 2- and 3-σ errors are represented as solid, dashed and dotted boxes, respectively. The data for β Cru f_2 shows that $\phi^{M}_{U\lambda} - \phi^{M}_{Q\lambda} = -\pi/2$, meaning that lines with open circles represent $-m$ modes and filled circles $+m$ modes. Similarly, dashed lines correspond to $\Phi_{\chi} = 25°$ and solid lines 115°. The amplitudes are presented on the bottom axis in terms of $z_{\ell\lambda}$ and $b_{\ell\lambda}$, which are derived from a stellar atmosphere model (Methods) and are dependent on ℓ and wavelength, λ, as well as $T_{\rm eff}$ and log(g). These values and their ratios for β Cru and the relevant wavelengths are given in Supplementary Table 5. Note that when $z_{\ell\lambda}/b_{\ell\lambda}$ is negative, as it is for $\ell = 4$, the solid and dashed lines are switched. The top axes show the amplitude ratios for $z_{\ell 460}$ and $b_{\ell 800}$.

demonstrate that, in some cases, favourable inclination and mode combinations could produce very large polarization amplitudes; this is particularly true for higher-order modes. Thus, even polarimetry at a precision of tens of ppm should be sufficient to restrict the allowed modes and/or inclination in other similar stars.

With the polarimetric data presented in the paper, β Crucis is currently the highest-mass β Cep star with such asteroseismic information. While these results can be improved by dedicated modelling including the interior rotation from the identified modes, our study reveals that combined time-series space photometry along with ground-based spectroscopy and polarimetry leads to a self-consistent solution for the modes and their identification. A crucial aspect for future applications to stars without line-profile variability data is that the polarimetry places stringent constraints on the inclination angle of the star. This is demonstrated by Fig. 6, which shows the reduction in the number of allowed solutions associated with just the polarimetric constraints from one mode, f_2.

The relative phases of the modes in polarimetry and photometry were crucial for applying the analytical model to f_2. Of the space-based photometric missions that have observed β Cru, only the TESS observations were sufficiently contemporaneous to facilitate this determination. TESS's improved precision over past photometric missions produced additional frequency identifications, and, as per our mode identification, many of these frequencies are likely to be higher-order modes, to which polarimetry is generally more sensitive. Therefore, if polarimetry is to be used to maximal effect in mode determination, it is urgent to acquire similar polarimetric data on other β Cep stars being observed by TESS during its mission, which has been extended through 2022 (ref. [40]).

There are a dozen known β Cep stars brighter than fifth magnitude ($m_V < 5$) with pulsation amplitudes larger than or similar to β Cru[41] to which this method can now be applied. Once a sufficient number of their interior structures are determined, main-sequence stellar evolution calculations can be calibrated and more accurately

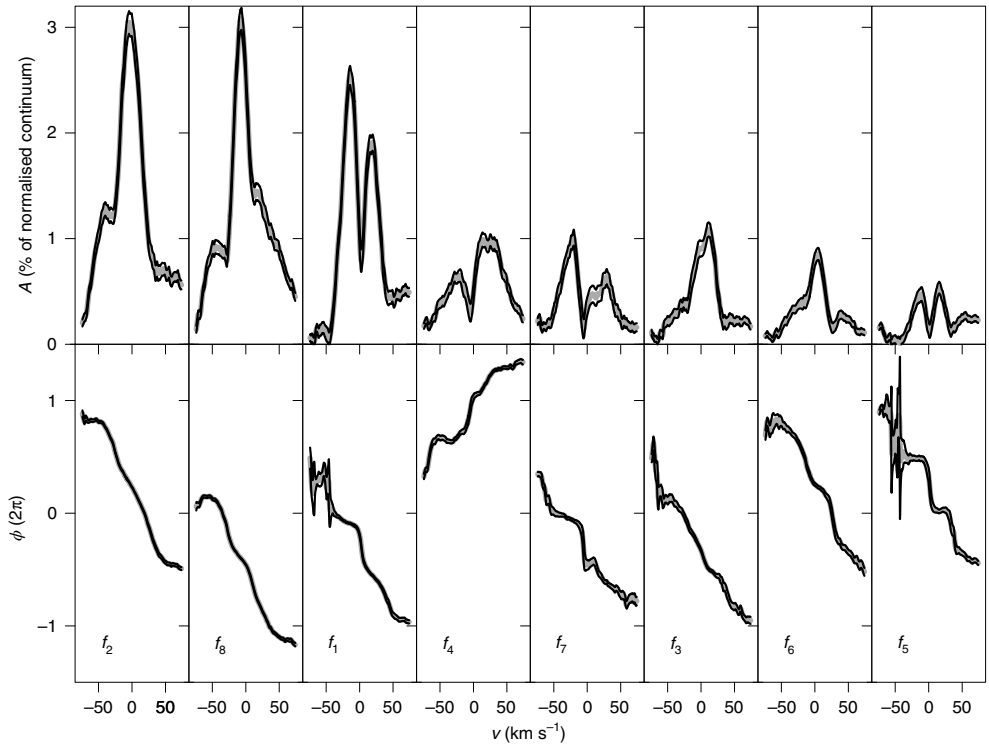

Fig. 5 | Line-profile analysis for β Cru. The residual Si III line at 4,552.6 Å from which the average profile was subtracted was fit with a linear multiperiodic oscillation model of the form $p_{\rm spec}(\lambda, t) = \sum_{i=1}^{8} A_{i,\lambda} \sin(2\pi f_i t + \phi_{i,\lambda})$ for the eight frequencies labelled in Table 1. The frequencies are shown here, left to right, in order of dominance. The thick grey line indicates the best linear least-squares fit and the area indicated by the thin black lines represents the 1σ uncertainty region. Modes with an upwards phase slope are zonal ($m = 0$) or retrograde ($m > 0$), while those with a downward phase slope are zonal ($m = 0$) or prograde ($m < 0$).

extrapolated to the stage before the core collapse, which in turn informs the spectral and chemical evolution theories of galaxies[42].

Methods

Archival time-series photometry and spectroscopy. Extensive time-series studies of β Cru have been performed based on high-resolution ground-based spectroscopy spread over 13 years (ref. [5]) and on WIRE (https://www.jpl.nasa.gov/missions/wide-field-infrared-explorer-wire) space photometry[31,32]. WIRE observed β Cru in June–July 1999 for a total of 17 days with a cadence of 10 Hz. For the current re-analyses, those WIRE data were re-reduced using the WIRE pipeline developed later in the mission[43] and binned to 120 s cadence. We refer to ref. [5] for details on the 13-year-long spectroscopic dataset of high-resolution spectroscopy, consisting of 1,193 high-resolution high-SNR spectra. These data led to the discovery of the spectroscopic binary nature of β Cru, with an orbital period of 5 years and a B2 V secondary. Clear line-profile variations were discovered and led to the detection of three oscillation frequencies. These are included in Table 1 and discussed further below. The combined WIRE and spectroscopic high-precision data analyses led to the conclusion[32] that the two dominant modes in the WIRE photometry with frequencies $f_1 \simeq 5.231\,{\rm d}^{-1}$ and $f_3 \simeq 5.477\,{\rm d}^{-1}$ are different from the dominant mode in the second moment of the line-profile variability, $f_2 \simeq 5.959\,{\rm d}^{-1}$. These three modes were found to be non-radial ($\ell \neq 0$), but aside from $\ell_1 = 1$ the identifications of ℓ_2 and ℓ_3 as well as all of m_1, m_2 and m_3 remained ambiguous.

Polarimetric observations. We have made 307 high-precision polarization observations of β Cru using the 3.9-m AAT at Siding Spring and the 60-cm telescope at Western Sydney University's (WSU) Penrith Observatory using HIPPI-2[25]; these observations were made between March 2018 and July 2019. A single observation was also made at UNSW Observatory in Sydney with a 35-cm Celestron C14 telescope using Mini-HIPPI (ref. [44]) in May 2016.

All the observations used Hamamatsu H10720-210 photo-multiplier tubes as the detectors. The operating procedures were standard[25], the instrument was always mounted at the Cassegrain focus and the instrument/telescope configuration details are summarized in Supplementary Table 1. A single sky (S) measurement was made adjacent to each target (T) measurement at each of the four position angles, PA = 0, 45, 90, 135°, in the pattern TSSTTSST. On a number of occasions, the observations were made back-to-back in a series stretching a few to several hours.

A small polarization due to the telescope mirrors shifts the zero-point offset of our observations. This is corrected for by reference to the straight mean of several observations of low-polarization standard stars, details of which are given in Supplementary Table 2. The position angle is calibrated by reference to literature measurements of high-polarization standards[25] listed in Supplementary Table 3.

Most of the observations were made using an SDSS g′ filter in which HIPPI-2 has a nominal (ultimate) precision per observation, $e_{\rm p}$, of 1.7 ppm on the AAT and 8.2 ppm on the WSU 60-cm telescope. Without a filter (clear) on the AAT this figure is 2.9 ppm; the equivalent figure for Mini-HIPPI on the UNSW 35-cm is 14.0 ppm (ref. [25]). To determine the error for any given measurement, we take the square root of the sum of $e_{\rm p}$ and the internal measurement error, $\sigma_{\rm p}$, which is the standard deviation of the polarization determined from each integration that makes up a measurement. Exposure times are selected so that $\sigma_{\rm p}$ is similar to $e_{\rm p}$. Some observations were made in poor weather, which has the effect of raising $\sigma_{\rm p}$ (from a lower photon count) and/or increasing the dwell time per observation (when scattered clouds are allowed to pass before beginning a new measurement). The dwell time is the total time for an observation, including sky exposures and dead time, between the start of the first measurement and the end of the last measurement in the PA sequence.

Without a filter, the instrument has a similar effective wavelength ($\lambda_{\rm eff}$) to the SDSS g′ filter, but a much wider band: ~350 to 700 nm, compared with ~400 to 550 nm. However, both the intrinsic and interstellar polarization will have a wavelength dependence, so the subsequent frequency and mode analysis is limited to the 274 SDSS g′ observations. The small variability in $\lambda_{\rm eff}$, and the modulation efficiency (Eff) within a run (as shown in Supplementary Table 1) is purely a result of taking account of airmass differences in the bandpass model. All of the observations were reduced using the standard procedures for HIPPI-class instruments[25].

New TESS photometry. NASA's TESS Mission[45] began performing a two-year near-all-sky survey in 2018 as part of its prime mission. The survey covered each hemisphere in 13 sectors, each lasting roughly 27 days, though there is appreciable sector overlap near the ecliptic pole so that some portions of the sky had longer periods of near-continuous coverage. Each sector was observed with 30-minute cadence, but a subset of pre-selected targets were observed at a shorter 2-minute cadence.

TESS observed β Cru in 2-minute cadence for 27 days during Sector 11 of Cycle 1; the observing dates for that sector cover 22 April 2019 to 21 May 2019 and

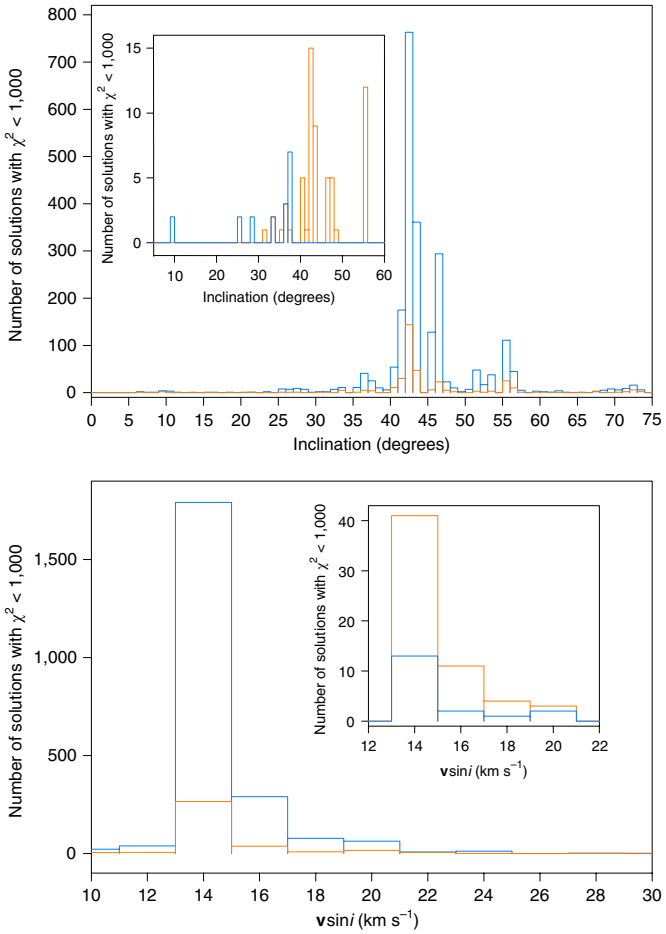

Fig. 6 | Distributions of β Cru's rotation axis inclination angle. Histograms of the rotation inclination angle (upper panel) and of the projected surface rotation velocity (lower panel) for all the solutions of the line-profile fits having $\chi^2 < 1{,}000$. Among all considered cases of $\ell \in [0, 4]$ for all eight modes detected in the spectroscopy (compare with Fig. 5), only solutions where the dominant mode in polarimetry has $\ell = 3$ (orange) or $\ell = 4$ (blue) fulfil $\chi^2 < 1{,}000$ so we exclude a lower degree for that mode. The insets show the subsets of solutions when imposing the stringent constraints on the inclination angle derived from the polarimetry for each of the possibilities shown in Fig. 4. This reveals the major gain in limiting the number of solutions from the inclination restrictions imported from the polarimetry.

thus overlap the ground-based polarimetric observations in time. We produced a light curve using the target pixel files produced by the TESS Science Processing Operations Center[46] using the procedure outlined in Nielsen et al.[47]. Effectively, we produced time series for each pixel and then derived an aperture photometry mask that minimized the mean absolute deviation figure of merit $q = \sum_{i=1}^{N-1} |f_{i+1} - f_i|$, where f_i is the flux at cadence i and N is the length of the time series. The resulting light curve was then detrended against the centroid pixel coordinates by fitting a second-order polynomial with cross terms, resulting in a light curve with modestly improved noise characteristics compared with the Science Processing Operations Center product. We note that, while the TESS image is saturated, the large postage stamp of 549 pixels effectively captures all electrons that overflow down the columns, and the stamp is far enough (200 pixels) from the edge of the detector to ensure that no electrons are lost. The TESS data release notes[48] do not identify this target as problematic, and we have confirmed that the count rate is within 1% of the level expected for a TESS magnitude of 2.82.

Joint frequency analysis. Our frequency analysis was motivated by the desire to take advantage of the numerous mutually supporting datasets available, rather than to try to analyse each fully independently and later combine those results. This joint analysis made use of light curves from WIRE, TESS, g′ band polarimetry, archival ground-based spectroscopy and archival Hipparcos data. In each case, we corrected times to BJD-2440000 and applied a high-pass filter to truncate frequencies below ~1 d^{-1}. Since we wished to conduct a joint analysis, and the different observation sets measured different physical quantities (relative flux in three different bands, polarization and velocity moments $\langle v \rangle$ and $\langle v^2 \rangle$), we scaled each light curve by dividing by its standard deviation to ensure that the relative dispersions of each were similar.

The algorithm we applied began with calculation of discrete Fourier transforms and amplitude spectra for each scaled light curve. In each case we used the same frequency grid [0, 10] d^{-1} with frequency resolution sufficient to 10 times oversample the longest time series. We then followed the methodology of Sturrock et al.[49] in constructing a joint amplitude spectrum from the two highest SNR photometric time series, WIRE and TESS, as

$$X = \left(\frac{2}{N_W} \times \frac{2}{N_T}\right)^{1/2} (F_W \circ F_T)^{1/2} \quad (1)$$

where N_W and N_T represent the number of points in the WIRE and TESS time series, respectively, and F_W and F_T the corresponding Fourier transforms. An advantage to this approach is its ability to handle alias and instrumental peaks; as these are different in each time series, their amplitudes are depressed in the joint spectrum.

The largest amplitude peak was identified in the joint amplitude spectrum and used as a starting point for sine-curve fits to each individual time series, including a fit to the full combined WIRE + TESS light curve. Each time series was then prewhitened by the frequency determined from its specific sinusoidal fit, a new joint WIRE + TESS amplitude spectrum was constructed and the process repeated until 50 frequencies had been identified and removed.

For this study, we then conservatively retained for further analysis only those frequencies for which SNR > 4 for 2 or more individual time series, as shown in Table 1. This process is intentionally conservative, with the goal of building a minimal rather than a maximal frequency list. Thus, the 6.877 d^{-1} peak visible in Fig. 2b does not appear in Table 1 because it is only significant in the TESS dataset (the frequency is detected in the WIRE light curve, but only with SNR ≈ 2.5). Similarly, for the Hipparcos time series, while we do detect f_3, whose presence was reported as 'marginal' by Cuypers et al.[32], it does not appear in our table because it fails to meet our SNR criterion.

Each individual light curve also produces a number of frequencies that fail to satisfy our SNR requirement. The majority of these are low-frequency peaks (<1 d^{-1}) that are presumably either due to a stellar process such as internal gravity waves, rotation or near-core convection, or to instrumental effects, and that are unique to a particular time series. Thus, to identify all of the peaks in each individual dataset that satisfy our SNR requirement, we remove a total of 23 frequencies. The residual amplitude spectrum shown in Fig. 2c is the result of removing those 23 frequencies from the TESS light curve.

We also confirmed by inspection of the final prewhitened amplitude spectra for the individual time series that no meaningful peaks remained in any of these. Finally, we fit in a least-squares sense a multicomponent sinusoidal model to each dataset using the frequencies, amplitudes and phases from the above algorithm as input values that are allowed to vary within a narrow range, and the results of that fit are used to finalize frequency determinations and estimate uncertainties. Using this process, we achieve improved fits to the first and second moment variations[5] thanks to the frequencies established from the combined space photometry.

Polarimetric mode identification. To make mode assignments using polarimetry we employ the analytical model of Watson[18]. This model assumes that deviations from spherical symmetry are small; it takes account of the effect of local changes in temperature and gravity on the light intensity, the effect of surface twist on changing **Q** and **U** in the plane of the sky and the changing projected area of a surface element. It neglects rotation effects, the effect of changes in the local temperature and gravity on the limb darkening function and changing polarization resulting from the changing surface normal.

In the reference frame of the stellar axis projected on the plane of the sky, the model[18] (denoted by ^{M}) uses the ratio of polarimetric amplitudes ($A^M_{U\lambda}/A^M_{Q\lambda}$) and the ratio of polarimetric to photometric amplitudes ($A^M_{Q\lambda}/A_\lambda$), along with the relative phases ($\phi^M_{U\lambda} - \phi^M_{Q\lambda}$ and $\phi^M_{Q\lambda} - \phi_\lambda$) to constrain the allowed modes (or uniquely identify a mode if the inclination, i, is precisely known). The wavelength-, λ-, dependent amplitudes depend primarily on geometry (although the polarimetric amplitudes are wavelength dependent, their ratio is not); the detail of the atmosphere is accounted for through only two parameters, the polarimetric scaling factor $z_{\ell\lambda}$ and photometric scaling factor $b_{\ell\lambda}$, determined by radiative transfer calculations (see the next section). Note that the wavelength dependence of the phases comes about only as a result of sign changes in the ratio $z_{\ell\lambda}/b_{\ell\lambda}$.

To determine these quantities for f_2 we rotate the measured polarization to align with the model frame, as demonstrated in Fig. 3. Algebraically, such rotation is accomplished, in general, by $\mathbf{Q}' = \mathbf{Q}\cos 2\theta - \mathbf{U}\sin 2\theta$ and $\mathbf{U}' = \mathbf{U}\cos 2\theta + \mathbf{Q}\sin 2\theta$, where 2θ is the rotation angle. In this instance, the rotation must result in $\phi^M_{Q\lambda} - \phi_\lambda = 0$ or π, with each solution corresponding to different modes. This results in θ corresponding to the stellar axis polarization position angle, Φ_χ; measured north over east, in this case 25 or 115 ± 3° (1σ errors).

Because polarization is a pseudo-vector (it has a magnitude and orientation, as opposed to a vector, which has a magnitude and a direction), the true position angle of the stellar axis will be either Φ_χ or $\Phi_\chi+\pi$, meaning it may also be 205 or $295\pm3°$. In the figure $\phi_U-\phi_Q\approx-\pi/2$ (-1.44 ± 0.24 rad)—only a value of $\pi/2$ or $-\pi/2$ is allowed—and this value means the polarization rotates counter-clockwise (north through east) on the plane of the sky with time, which determines the sign of m for a given ℓ and i. $A^M_{Q\lambda}$ and $A^M_{U\lambda}$ correspond to the amplitudes of the rotated Stokes parameters in Fig. 3b,c.

In the case of a radial mode, the mode symmetry results in no net polarization change over the stellar disk. Less obviously, under the assumptions of the analytical model, a dipole mode ($\ell=1$) also produces no net polarization; this is a consequence of polarization measuring orientation rather than direction, and thus distortions at opposite hemispheres cancelling[16–18]. Only modes of order $\ell=2$ and 3 have previously been calculated using the analytical model. Following Watson's[18] approach, we also made calculations for $\ell=4$, which we present here; the work required additional angular momentum transformation matrix elements, which are given in Supplementary Table 4. Despite potentially larger polarimetric amplitudes, larger ℓ values are less likely to be detected, as a consequence of smaller photometric amplitudes (Supplementary Information). Therefore, we infer f_2, and indeed any mode, detected in β Cru here with polarimetry must have $\ell=2$, 3 or 4. Using the measured amplitudes plotted against the model predictions in Fig. 4, we can place tighter constraints on the allowed modes in terms of ℓ, m and i. The results are shown for both the TESS ($\lambda=800$ nm) and WIRE ($\lambda=600$ nm) photometric amplitudes. Given the decade-long gap between the polarimetric and WIRE datasets, we rely on the TESS phasing for both. Using the TESS photometry, the allowed modes and inclinations (3σ errors) are: $(2,-2)$, $i=7^{+4}_{-2}{}^\circ$; $(3,+1)$, $i=66^{+9}_{-1}{}^\circ$; $(3,-2)$, $i=20^{+8}_{-4}{}^\circ$; $(3,-3)$, $i=37^{+18}_{-8}{}^\circ$; $(4,-2)$, $i=11^{+5}_{-3}{}^\circ$; and $(4,-4)$, $i=27^{+13}_{-6}{}^\circ$. The $(3,+1)$ solution corresponds to $\Phi_\chi=115\pm8°$, the others to $\Phi_\chi=25\pm8°$. We conservatively adopted 3σ errors here for i and Φ_χ to allow for $\phi_U-\phi_Q$ not being exactly $-\pi/2$, the possibility that the amplitudes are damped by zero-point or inter-run calibration offsets, as well as effects not included in the analytical model, and the fact that our calculations are monochromatic but the observations broadband.

Polarized radiative transfer. The analysis of Watson[18] provides expressions for the amplitude of pulsations in intensity and polarization that depend on the details of the stellar atmosphere model only through a pair of values (for a given ℓ and wavelength λ) $b_{\ell\lambda}$ and $z_{\ell\lambda}$ that are derived from the viewing angle ($\mu=\cos\theta$) dependence of the modelled intensity and polarization. A small number of these values, mostly for ultraviolet wavelengths, are tabulated by Watson[18]. We calculated new values using ATLAS9 stellar atmosphere models and the SYNSPEC/VLIDORT stellar polarization code[26,27,50], which is a version of the SYNSPEC spectral synthesis code[51] that we have modified to do polarized radiative transfer using the VLIDORT code[52]. As a check, we recalculated the values listed by Watson[18] for a star of effective temperature, $T_{\rm eff}=23{,}000$ K and surface gravity, $\log(g)=3.6$ and found good agreement. We calculated new values for a star of $T_{\rm eff}=27{,}000$ K and $\log(g)=3.6$ appropriate for β Cru[53]. The calculated values are given in Supplementary Table 5.

Mode identification from combined spectroscopy and polarimetry. We revisited the archival time-series spectroscopy, described in detail by Aerts et al.[5], consisting of 1,193 high-resolution (binned to $\Delta\lambda=0.03$ Å) high signal-to-noise (SNR ∈ [250, 750]) spectra covering the Si III $\lambda\lambda$4552, 4568, 4574 Å triplet. The time base spans 13 years but the temporal coverage is sparse; the data were taken on 25 individual nights, with intense monitoring during a single night twice, and on two, three and four consecutive nights once each. These data led to the discovery of the spectroscopic binarity of the star, revealing an eccentric system with an orbital period of ~5 yr and a B2 V secondary with $T_{\rm eff}=22{,}000$ K, $\log(g)\simeq4.0$, delivering ~8% of the flux[5] (see the Supplementary Information for additional information on the companion).

Here we used the orbit-subtracted line profiles of the Si III triplet to perform mode identification with the pixel-by-pixel method, also known as the Fourier Parameter Fit method[37]. This method had not yet been applied to β Cru's complex line-profile variability. It can handle more modes than the moment method because it is based on the periodic variability in each of the wavelength bins belonging to the spectral lines, rather than using integrated quantities across the profiles as is the case for the moment method[54]. We fixed the frequencies found in the space photometry according to Table 1 to test which of those have significant amplitude A_λ and phase ϕ_λ across each of the three Si III lines. The outcome is consistent for each of the three lines of the Si triplet and is displayed in Fig. 5 for the deepest of the three lines. Its central laboratory wavelength occurs at 4552.6 Å and the variability in this line reveals eight of the eleven frequencies as significant, labelled as such in Table 1.

Spectroscopic mode identification with the Fourier Parameter Fit method using the code FAMIAS[38] was performed for the eight modes by treating them separately from their amplitude and phase behaviour shown in Fig. 5, adopting a grid-based approach. FAMIAS relies on a user-provided value of the effective temperature and gravity of the star to predict its limb darkening for the considered spectral line. For each of the eight modes, we varied the degree in $\ell\in[0,4]$ and the azimuthal order $m\in[-\ell,\ell]$. This mode-identification method is known to provide more robust results for the azimuthal order than for the mode degree, particularly for zonal modes revealing a step-like behaviour in the phase across the line profile[8]. The local amplitudes of the modes were allowed to vary from 1 to 50 km s^{-1} in steps of 1 km s^{-1}, while the inclination angle of the rotation axis varied from 2° to 75° in steps of 2° and the projected rotation velocity $v\sin i$ from 10 to 40 km s^{-1} in steps of 2 km s^{-1}. An additional free parameter needed to fit line profiles is the so-called intrinsic line broadening, here approximated as a Gaussian with width ranging from 10 to 30 km s^{-1} in steps of 2 km s^{-1}. We then find the acceptable solutions for the spectroscopic mode identification by extracting those with one common value for i and $v\sin i$. This produces thousands of options, some of which are listed in Supplementary Table 6. The results for i and $v\sin i$ for all the solutions having $\chi^2\leq1000$ are shown in Fig. 6. Only solutions with $\ell=3$ or 4 for the dominant mode in polarimetry remain, in full agreement with spectroscopic mode identification from the moment method[6].

Subsequently, we apply three restrictions from the polarimetry. As a first restriction, we demand compliance with the allowed inclination angles for each of the options for the dominant mode with frequency f_2 (Fig. 3). This restricts the solution space to 98 options whose i and $v\sin i$ are shown in the insets in Fig. 6. It can be seen that $v\sin i$ is very well constrained thanks to this condition imposed by the dominant mode in the polarimetry. As a second condition from polarimetry, we require that f_6 has a mode with a measurable A^M_U (>2 ppm), since we have a clear detection for this, which whittles the viable options down to 30. Finally, we eliminate any option with a significant predicted amplitude that is not detected; for this condition we conservatively set the threshold at 5.5 ppm; this value is chosen to be 0.5 ppm above the top of the noise floor seen in Fig. 2e and just below the detected amplitude of f_2 in U/I. There are eight options that strictly meet these criteria, and another one that could when one considers nominal errors.

Together with the predicted polarimetric amplitudes, the final solutions are given in Supplementary Table 7, listed in order of highest probability in complying with all constraints from spectroscopy and polarimetry together. Notably, the mode with frequency f_5 must be a zonal mode ($m_5=0$) from its zero amplitude in the line centre and its step function in phase[54], as shown in the lower right panel of Fig. 5. The best solution (solution A in Supplementary Table 7) identifies f_2 as a $(3,-3)$ mode and f_1 as $(1,-1)$, for an inclination angle of $46°\pm2°$ and $v\sin i$ 16 ± 2 km s^{-1}. Furthermore, since f_2 and f_8 are found to belong to the same multiplet, $f_2-f_8=0.0431$ d^{-1}, and this will allow the deduction of the envelope rotation rate, at the position inside the star where these modes have their dominant probing power. A concrete value can only be derived from dedicated asteroseismic models[3].

Asteroseismic models. To get a first assessment of stellar models compliant with our mode identification, we apply a neural network trained on a large grid of stellar models covering masses from 2 to 20 $M_\odot$ and treating zonal modes of degree 0, 1 and 2 (ref. [39]). Since this neural network does not predict modes of higher degree, we fed it with the frequency f_1 as a dipole mode and assumed f_5 to be a quadrupole zonal mode, as found for the best solution (A) for the mode identification. Although f_1 is not zonal, the frequency shift induced by rotation is very small, of order 0.02 d^{-1} as deduced from f_2 and f_8. We explicitly checked that this frequency difference does not affect the results discussed below.

The neural network only allows us to use zonal modes of $l\leq2$. Although some of the solutions in Supplementary Table 7 list f_3 and f_4 as zonal modes, we do not wish to rely on their identification because these modes' amplitude distribution is not characteristic of such a mode, in comparison with the one for f_5 that is symmetrical and drops to zero value in the line centre (Fig. 5). We thus rely on the most secure identification for the two zonal modes, that is, f_1 and f_5. Without any further constraint, the neural network delivers model solutions for a star with too high a mass at the edge of the model grid. We therefore used additional constraints from spectroscopy and from the Hipparcos parallax to place β Cru in the Hertzsprung–Russell diagram. The bolometric luminosity was computed from the spectroscopic $T_{\rm eff}$ and $\log(g)$ (ref. [53]) and combined with an estimate for the reddening, $E(B-V)\simeq0.03$ mag, from the polarimetry (Supplementary Information) to derive the reddening corrected apparent bolometric magnitude[55], and subsequently determine the luminosity using the Hipparcos parallax. The 1σ and 3σ results are graphically depicted in Supplementary Fig. 4, along with evolutionary tracks for masses, $M=12$, 14, 16 and 18 $M_\odot$, for various levels of initial (hydrogen mass fraction, metallicity) chemical composition (X,Z), convective-core overshooting, $f_{\rm ov}$, in an exponentially decaying diffusive description, and envelope mixing $D_{\rm mix}$ (ref. [56]).

We used the position of β Cru in the Hertzsprung–Russell diagram to restrict the neural network, initially to the still rather broad mass range [9, 18] $M_\odot$ (grey dots in Supplementary Fig. 5) and then to the acceptable mass range deduced from the 3σ position box in the Hertzsprung–Russell diagram, that is, [12, 16] $M_\odot$ (blue dots). For both applications, we fixed the initial chemical composition to the observed values of the metallicity and helium mass fraction, $Z=0.014$ and $Y=0.268$ respectively[53], resulting in an initial hydrogen mass fraction of $X=0.718$. We fixed this initial chemical composition given the tight (M,Z), $(f_{\rm ov},Z)$ and $(D_{\rm mix},Z)$ relations[56]. The outcome in Supplementary Fig. 5 reveals that the best solution occurs at a mass between 14 and 15 $M_\odot$. The evolutionary stage is well

determined by the estimate of the hydrogen mass fraction in the convective core, $X_c \in [0.30, 0.33]$. The internal mixing parameters are not constrained, which is not surprising given we only modelled two modes[39]. Relying on $X_c \in [0.30, 0.33]$ and allowing for the full ranges for the convective-core overshooting and envelope mixing covered by the grid, we find the star to have an age between 9.7 and 12.8 million years and a convective-core mass between 25% and 32% of its mass. This is in good agreement with the need for higher-than-standard core masses as derived from eclipsing binaries in this mass range[57]. The neural network solution places the star in between the two evolutionary tracks indicated in black lines in Supplementary Fig. 4.

We find the radius of the star to fall in the range from 7.3 to 8.9 $R_\odot$. This is slightly larger than implied by the angular diameter as measured by intensity interferometry[58] if using the new Hipparcos reduction[59] for parallax, $6.6 \pm 0.6\,R_\odot$, but in good agreement if using the original Hipparcos parallax determination[60], $8.2 \pm 0.5\,R_\odot$. Both our mass and radius estimates are in agreement with earlier values based on multicolour photometry[61]. The range for the radius, combined with the inclination and spectroscopic estimate of $v\sin i \simeq 16\,\mathrm{km\,s^{-1}}$, lead to an equatorial rotation velocity of $\simeq 22\,\mathrm{km\,s^{-1}}$ and a surface rotation period between 13 and 17 days. The corresponding rotation frequency does not occur prominently in the TESS data, that is, we do not see any conclusive evidence of rotational modulation. Such slow surface rotation is quite common among β Cep pulsators[53,61]. Various physical phenomena can explain an effective slow-down during the star's evolution[3], amongst which is magnetic braking. In the case of β Cru, the presence of a magnetic field is inconclusive so far[62]. Additional constraints on the internal rotation can in principle be derived. This requires dedicated future asteroseismic modelling based on all identified modes. Methods to do so have not yet been developed for cases with dominant $\ell > 2$ modes as found here.

Data availability

The new data that support the plots within this paper and other findings of this study will be available from the VizieR service upon print publication. All other data analysed in this work come from public repositories; where this is the case, the origin of the data is indicated in the text.

Code availability

Our polarimetric modelling code is based on the publicly available ATLAS9, SYNSPEC and VLIDORT codes. Our modified version of SYNSPEC is available on request. The spectroscopic mode identification was performed with the software package FAMIAS available from https://fys.kuleuven.be/ster/Software/famias/famias, applied to the time-series spectroscopy available from https://fys.kuleuven.be/ster/Software/helas/helas. The neural network is available from https://github.com/l-hendriks/asteroseismology-dnn. The joint frequency analysis was conducted using a custom MATLAB package that is available on request.

Received: 27 July 2020; Accepted: 30 September 2021;
Published online: 6 December 2021

References

1. Hekker, S. & Christensen-Dalsgaard, J. Giant star seismology. *Astron. Astrophys. Rev.* **25**, 1 (2017).
2. García, R. A. & Ballot, J. Asteroseismology of solar-type stars. *Living Rev. Sol. Phys.* **16**, 4 (2019).
3. Aerts, C., Mathis, S. & Rogers, T. M. Angular momentum transport in stellar interiors. *Annu. Rev. Astron. Astrophys.* **57**, 35–78 (2019).
4. Pamyatnykh, A. A. Pulsational instability domains in the upper main sequence. *Acta Astron.* **49**, 119–148 (1999).
5. Aerts, C. et al. Evidence for binarity and multiperiodicity in the β Cephei star β Crucis. *Astron. Astrophys.* **329**, 137–146 (1998).
6. Briquet, M. & Aerts, C. A new version of the moment method, optimized for mode identification in multiperiodic stars. *Astron. Astrophys.* **398**, 687–696 (2003).
7. Aerts, C. Probing the interior physics of stars through asteroseismology. *Rev. Mod. Phys.* **93**, 015001 (2021).
8. Aerts, C., Christensen-Dalsgaard, J. & Kurtz, D. W. *Asteroseismology* (Springer-Verlag, 2010).
9. Aerts, C. et al. Asteroseismology of the β Cep star HD 129929. I. Observations, oscillation frequencies and stellar parameters. *Astron. Astrophys.* **415**, 241–249 (2004).
10. Handler, G. et al. Asteroseismology of the β Cephei star 12 (DD) Lacertae: photometric observations, pulsational frequency analysis and mode identification. *Mon. Not. R. Astron. Soc.* **365**, 327–338 (2006).
11. Briquet, M. et al. Multisite spectroscopic seismic study of the β Cep star V2052 Ophiuchi: inhibition of mixing by its magnetic field. *Mon. Not. R. Astron. Soc.* **427**, 483–493 (2012).
12. Handler, G. et al. Asteroseismology of hybrid pulsators made possible: simultaneous MOST space photometry and ground-based spectroscopy of γ Peg. *Astrophys. J. Lett.* **698**, L56–L59 (2009).
13. Stokes, G. G. On the composition and resolution of streams of polarized light from different sources. *Trans. Camb. Philos. Soc.* **9**, 399–416 (1851).
14. Clarke, D. *Stellar Polarimetry* (Wiley, 2010).
15. Chandrasekhar, S. On the radiative equilibrium of a stellar atmosphere. X. *Astrophys. J.* **103**, 351–370 (1946).
16. Odell, A. P. Possible polarization effects in the β Cephei stars. *Publ. Astron. Soc. Pac.* **91**, 326–328 (1979).
17. Stamford, P. A. & Watson, R. D. Polarization models for hot nonradial pulsators. *Acta Astron.* **30**, 193–214 (1980).
18. Watson, R. D. Mode constraints on nonradial pulsations from polarization data. *Astrophys. Space Sci.* **92**, 293–306 (1983).
19. Schafgans, J. J. & Tinbergen, J. An attempt to detect non-radial pulsation in β Cephei. *Astron. Astrophys. Suppl.* **35**, 279–280 (1979).
20. Clarke, D. Polarization measurements of β Cep stars. *Astron. Astrophys.* **161**, 412–416 (1986).
21. Elias, N. M. II, Koch, R. H. & Pfeiffer, R. J. Polarimetric measures of selected variable stars. *Astron. Astrophys.* **489**, 911–921 (2008).
22. Odell, A. P. Nonradial pulsation detected through polarization variation in BW Vul. *Astrophys. J. Lett.* **246**, L77–L80 (1981).
23. Aerts, C. et al. Mode identification of the β Cephei star BW Vulpeculae. *Astron. Astrophys.* **301**, 781–787 (1995).
24. Bailey, J. et al. A high-sensitivity polarimeter using a ferro-electric liquid crystal modulator. *Mon. Not. R. Astron. Soc.* **449**, 3064–3073 (2015).
25. Bailey, J., Cotton, D. V., Kedziora-Chudczer, L., De Horta, A. & Maybour, D. HIPPI-2: a versatile high-precision polarimeter. *Publ. Astron. Soc. Aust.* **37**, e004 (2020).
26. Cotton, D. V. et al. Polarization due to rotational distortion in the bright star Regulus. *Nat. Astron.* **1**, 690–696 (2017).
27. Bailey, J., Cotton, D. V., Howarth, I. D., Lewis, F. & Kedziora-Chudczer, L. The rotation of α Oph investigated using polarimetry. *Mon. Not. R. Astron. Soc.* **494**, 2254–2267 (2020).
28. Cotton, D. V. et al. The linear polarization of southern bright stars measured at the parts-per-million level. *Mon. Not. R. Astron. Soc.* **455**, 1607–1628 (2016).
29. Pedersen, M. G. et al. Diverse variability of O and B stars revealed from 2-minute cadence light curves in sectors 1 and 2 of the TESS mission: selection of an asteroseismic sample. *Astrophys. J. Lett.* **872**, L9 (2019).
30. Pigulski, A. & Pojmański, G. β Cephei stars in the ASAS-3 data. I. Long-term variations of periods and amplitudes. *Astron. Astrophys.* **477**, 907–915 (2008).
31. Buzasi, D. Asteroseismic Results from WIRE. In *Astronomical Society of the Pacific Conference Series* Vol. 259 (eds Aerts, C. et al.) 616–619 (ASP, 2002).
32. Cuypers, J. et al. Multiperiodicity in the light variations of the β Cephei star β Crucis. *Astron. Astrophys.* **392**, 599–603 (2002).
33. Bailey, J. et al. Polarization of hot Jupiter systems: a likely detection of stellar activity and a possible detection of planetary polarization. *Mon. Not. R. Astron. Soc.* **502**, 2331–2345 (2021).
34. Dziembowski, W. Light and radial velocity variations in a nonradially oscillating star. *Acta Astron.* **27**, 203–211 (1977).
35. Briquet, M. et al. Ground-based observations of the β Cephei CoRoT main target HD 180 642: abundance analysis and mode identification. *Astron. Astrophys.* **506**, 269–280 (2009).
36. Handler, G. Confirmation of simultaneous p and g mode excitation in HD 8801 and γ Peg from time-resolved multicolour photometry of six candidate 'hybrid' pulsators. *Mon. Not. R. Astron. Soc.* **398**, 1339–1351 (2009).
37. Zima, W. A new method for the spectroscopic identification of stellar non-radial pulsation modes. I. The method and numerical tests. *Astron. Astrophys.* **455**, 227–234 (2006).
38. Zima, W. FAMIAS User Manual. *Commun. Asteroseismol.* **155**, 17–121 (2008).
39. Hendriks, L. & Aerts, C. Deep learning applied to the asteroseismic modeling of stars with coherent oscillation modes. *Publ. Astron. Soc. Pac.* **131**, 108001 (2019).
40. Coffey, V. C. TESS: the little satellite with a big job. *Opt. Photonics News* **31**, 22–29 (2020).
41. Stankov, A. & Handler, G. Catalog of galactic β Cephei stars. *Astrophys. J. Suppl.* **158**, 193–216 (2005).
42. Bernardi, M. et al. Early-type galaxies in the Sloan Digital Sky Survey. IV. Colors and chemical evolution. *Astrophys. J.* **125**, 1882–1896 (2003).
43. Bruntt, H., Kjeldsen, H., Buzasi, D. L. & Bedding, T. R. Evidence for granulation and oscillations in procyon from photometry with the WIRE satellite. *Astrophys. J.* **633**, 440–446 (2005).
44. Bailey, J., Cotton, D. V. & Kedziora-Chudczer, L. A high-precision polarimeter for small telescopes. *Mon. Not. R. Astron. Soc.* **465**, 1601–1607 (2017).
45. G. R, Ricker. et al. Transiting Exoplanet Survey Satellite (TESS). *Proc. SPIE* **9143**, 914320 (2014).
46. Jenkins, J. M. (ed.) *Kepler Data Processing Handbook*: *KSCI-19081-002* (NASA Ames Research Center, 2017).
47. Nielsen, M. B. et al. TESS asteroseismology of the known planet host star λ^2 Fornacis. *Astron. Astrophys.* **641**, A25 (2020).

48. Fausnaugh, M. M. et al. *TESS Data Release Notes: Sector 11, DR16* (STScI, 2019).
49. Sturrock, P. A., Scargle, J. D., Walther, G. & Wheatland, M. S. Combined and comparative analysis of power spectra. *Sol. Phys.* **227**, 137–153 (2005).
50. Bailey, J., Cotton, D. V., Kedziora-Chudczer, L., De Horta, A. & Maybour, D. Polarized reflected light from the Spica binary system. *Nat. Astron.* **3**, 636–641 (2019).
51. Hubeny, I., Stefl, S. & Harmanec, P. How strong is the evidence of superionization and large mass outflows in B/Be stars? *Bull. Astron. Inst. Czechoslov* **36**, 214–230 (1985).
52. Spurr, R. J. D. VLIDORT: a linearized pseudo-spherical vector discrete ordinate radiative transfer code for forward model and retrieval studies in multilayer multiple scattering media. *J. Quant. Spectrosc. Radiat. Transf.* **102**, 316–342 (2006).
53. Morel, T., Hubrig, S. & Briquet, M. Nitrogen enrichment, boron depletion and magnetic fields in slowly-rotating B-type dwarfs. *Astron. Astrophys.* **481**, 453–463 (2008).
54. Telting, J. H., Aerts, C. & Mathias, P. A period analysis of the optical line variability of β Cephei: evidence for multi-mode pulsation and rotational modulation. *Astron. Astrophys.* **322**, 493–506 (1997).
55. Pedersen, M. G., Escorza, A., Pápics, P. I. & Aerts, C. Recipes for bolometric corrections and Gaia luminosities of B-type stars: application to an asteroseismic sample. *Mon. Not. R. Astron. Soc.* **495**, 2738–2753 (2020).
56. Moravveji, E., Aerts, C., Pápics, P. I., Triana, S. A. & Vandoren, B. Tight asteroseismic constraints on core overshooting and diffusive mixing in the slowly rotating pulsating B8.3V star KIC 10526294. *Astron. Astrophys.* **580**, A27 (2015).
57. Tkachenko, A. et al. The mass discrepancy in intermediate- and high-mass eclipsing binaries: the need for higher convective core masses. *Astron. Astrophys.* **637**, A60 (2020).
58. Hanbury Brown, R., Davis, J. & Allen, L. R. The angular diameters of 32 stars. *Mon. Not. R. Astron. Soc.* **167**, 121–136 (1974).
59. van Leeuwen, F. Validation of the new Hipparcos reduction. *Astron. Astrophys.* **474**, 653–664 (2007).
60. Perryman, M. A. C. et al. The Hipparcos Catalogue. *Astron. Astrophys.* **500**, 501–504 (1997).
61. Hubrig, S. et al. Discovery of magnetic fields in the β Cephei star ξ^1 CMa and in several slowly pulsating B stars. *Mon. Not. R. Astron. Soc.* **369**, L61–L65 (2006).
62. Hubrig, S. et al. New magnetic field measurements of β Cephei stars and slowly pulsating B stars. *Astron. Nachr.* **330**, 317–329 (2009).

Acknowledgements

This research has made use of the SIMBAD database and VizieR catalogue access tool, operated at CDS (Strasbourg, France). This research has made use of NASA's Astrophysics Data System. We thank the Director of Siding Spring Observatory, C. Lidman, for his support of the HIPPI-2 project on the AAT. We thank M. Filipovic for providing access to the Penrith Observatory. D.V.C. would also like to thank M. Filipovic and B. Carter for their support of his initially unfunded research on this project in the form of adjunct positions at WSU and USQ. We thank N. Cohen, G. Santucci and D. Maybour for assisting with the observations. We thank Wm. B. Weaver for useful comments on the manuscript. Funding for the construction of HIPPI-2 was provided by UNSW through the Science Faculty Research Grants Program (J.B.). Part of the research leading to these results has received funding from the European Research Council under the European Union's Horizon 2020 research and innovation programme by means of a European Research Council AdG to C.A. (grant agreement No. 670519: MAMSIE). This research was supported in part by the National Science Foundation under Grant No. NSF PHY-1748958 (M.G.P.). D.L.B. acknowledges support from the TESS Guest Investigator Program through award NNH17ZDA001N-TESS.

Author contributions

All authors contributed to the discussion and drafting of the final manuscript. D.V.C., D.L.B., C.A., J.B., D.S., M.G.P., P.D.C., L.K.-C. and A.D.H. contributed to observing proposals and/or scheduling. D.V.C., J.B., D.L.B., A.D.H., L.K.-C., F.L. and S.P.M. carried out polarimetric observations. In addition, the following authors made specific contributions to the work: D.V.C. initiated the work, contributed the polarimetric data processing and analysis, calculations of and comparisons with the analytical model, investigated binary effects, the interstellar polarization and co-ordinated the observations and analysis. D.L.B. carried out the frequency analysis and contributed analysis of asteroseismic data. C.A. analysed the spectroscopic data and carried out the associated mode identification, as well as the asteroseismic modelling. J.B. contributed the polarized radiative transfer modelling, investigated binary effects and aided with interpretation of the analytical model. S.B. computed theoretical stellar models and pulsation modes for the asteroseismic modelling and ran the neural network. M.G.P. computed bolometric corrections and the luminosity of β Cru, based on its spectroscopic properties. D.S. helped facilitate the initial collaboration and provided valuable context for the work.

Competing interests

The authors declare no competing interests.

Additional information

Supplementary information The online version contains supplementary material available at https://doi.org/10.1038/s41550-021-01531-9.

Correspondence and requests for materials should be addressed to Daniel V. Cotton or Derek L. Buzasi.

Peer review information *Nature Astronomy* thanks Dietrich Baade, Swetlana Hubrig and the other, anonymous, reviewer(s) for their contribution to the peer review of this work.